Decoupling the characteristics of magnetic nanoparticles for ultrahigh sensitivity

Decoupling the Characteristics of Magnetic Nanoparticles for Ultrahigh Sensitivity

Mohammad Suman Chowdhury[1], Enja Laureen Rösch[1], Daniel Arenas Esteban[2], Klaas-Julian Janssen[1], Florian Wolgast[1], Frank Ludwig[1], Meinhard Schilling[1], Sara Bals[2], Thilo Viereck[1], Aidin Lak[1*]

[1]Institute for Electrical Measurement Science and Fundamental Electrical Engineering and Laboratory for Emerging Nanometrology (LENA), TU Braunschweig, Hans-Sommer-Str. 66, Braunschweig, 38106, Germany

[2]EMAT, University of Antwerp, Groenenborgerlaan 171, B-2020 Antwerp, Belgium

KEYWORDS: *Magnetic nanomarkers, Zinc Cobalt Ferrite nanocubes, Brownian relaxation, Magnetic immunoassays, Magnetic particle spectroscopy, Catechol-PEG ligand.*

ABSTRACT:

Immunoassays exploiting magnetization dynamics of magnetic nanoparticles are highly promising for mix-and-measure, quantitative, and point-of-care diagnostics. However, how single-core magnetic nanoparticles can be employed to reduce particle concentration and concomitantly maximize assay sensitivity is not fully understood. Here, we design monodisperse Néel and Brownian relaxing magnetic nanocubes (MNCs) of different sizes and compositions. We provide insights into how to decouple physical properties of these MNCs to achieve ultrahigh sensitivity. We find that tri-component-based $Zn_{0.06}Co_{0.80}Fe_{2.14}O_4$ particles, with out-of-phase to initial magnetic susceptibility χ''/χ_0 ratio of 0.47 out of 0.50 for magnetically blocked ideal particles, show the ultrahigh magnetic sensitivity by providing rich magnetic particle spectroscopy (MPS) harmonics spectrum despite bearing lower saturation magnetization than di-component $Zn_{0.1}Fe_{2.9}O_4$ having high saturation magnetization. The $Zn_{0.06}Co_{0.80}Fe_{2.14}O_4$ MNCs, coated with catechol-based polyethylene glycol ligands, measured by our benchtop MPS show three orders of magnitude better particle LOD than that of commercial nanoparticles of comparable size.

INTRODUCTION:

Magnetic particle spectroscopy (MPS)-based magnetic immunoassays (MIAs) hold great promises for a rapid and simple detection of small molecules and biomolecules including virus, antibody, and RNA/DNA by offering a wash-free, mix and measure, and cost-effective detection concepts.[1–4] While the MIAs can significantly benefit from custom-designed nanomarkers with optimal magnetic and colloidal properties, yet commercial magnetic nanomarkers are widely being used that do not offer high sensitivity and specificity.[5,6] Both sensitivity and specificity are the true challenges that remain to be addressed ahead of MIAs before getting into the daily point-of-need applications, such as lateral flow assays. Furthermore, the complex interplays between critical magnetic properties such as saturation magnetization, magnetic anisotropy, and magnetic relaxation mechanism have to come together in magnetic nanomarkers. Consequently, these multiparametric complexities impede making a tangible progress in the field of MIAs.

Importantly, MPS-MIAs are based on the nonlinear response of magnetic nanoparticles (MNPs) to moderate alternating current (ac) magnetic fields, resulting in a spectrum with higher harmonics. The MIAs exclusively rely on Brownian relaxation mechanism of MNPs, which depends on hydrodynamic size of the particles. Medium viscosity also influences the Brownian relaxation; however, it is cancelled out when a control sample is measured. Therefore, upon a molecular

binding between MNPs and targeting analytes, the particle hydrodynamic volume increases, which leads to a change in the MPS spectrum. Besides, to push the limit of particle detection and assay sensitivity, particles should have high saturation magnetisation M_s, high magnetic moment *m*, and high magnetic anisotropy constant *K*. Of note, the relationship between particle detection sensitivity and MIAs sensitivity is directly proportional.[7,8] However, having all these complex characteristics in one particle system often comes with contradictions. The doping of iron oxide with a highly anisotropic cobalt results in a high *K*, but this comes with a reduction in M_s.[9–11] In contrast, the zinc doping triggers the opposite trend.[12] Thus, the binary metal oxides of iron with either cobalt or zinc are not optimal choices for MIAs, suggesting doping of both the ions in one particle to find the optimal properties. However, synthesis of ternary metal oxides comes with a trade-off between size, size and shape uniformity, and composition.[9,10,12] The existing synthesis protocols offer either an appropriate particle size or an optimal particle composition and hardly both.[13–15] In addition, these ternary nanoparticles are either below 20 nm or above 30 nm, limiting their utility for MIAs. Single-core particles < 20 nm do not provide large enough magnetic moment for highly sensitive assays. When they are > 30 nm they strongly interact via magnetic dipole-dipole interactions and are not colloidally stable.

The colloidal stability of magnetic nanoparticle suspensions is another crucial aspect that dictates the fate of the nanoparticles. Nanoparticles that are colloidally stable, monodisperse, and uniform in shape bear significant advantages over particles that are colloidally unstable, polydisperse, and irregularly shaped.[16] Most relevantly for MIAs, only colloidally stable nanoparticles are transferrable to aqueous medium. However, it is crucial not to trade off with the single particle resolution of the bio-functional particles, meaning no multi-core particles while transferring them to water. Besides, it is equally important to keep the hydrodynamic volume of the particles as low as possible after transferring them to water to detect minimal amount of analytes binding, because the lower the hydrodynamic volume of a particle is the higher will be its sensitivity towards analytes. It is therefore an absolute must to integrate the set of aforementioned physicochemical properties into a particle system that can efficiently be transferred to water with a high yield. We hypothesize that doping of a right amount of Co and Zn, which can, simultaneously, adjust the size of the particles, tune the amorphous and crystalline structures, and yield higher sensitivity, will lead to a high-performance magnetic nanomarkers. Structurally, when particles of same size are compared, cubic particles can have more surface area and thus have a higher loading of functional polymers and bio-markers than their spherical counterparts. However, we rule out cubic Fe_3O_4 particles based on previous investigations showing that purely Fe_3O_4 nanoparticles, despite having ≈ 20 nm diameter, follow Néel relaxation.[16–19] In addition, we rule out cubic Fe_3O_4 particles > 20 nm in diameter because strong interparticle magnetic interactions lead to particle aggregation.[16,20] Although Guardia et al. have demonstrated how *in situ* ligand exchange method can be exploited to address the particle aggregation, it remains a major challenge to preserve the single particle resolution in aqueous media.[21] Instead, alternative ternary nanoparticles composing of Zn, Co, Fe with sizes < 25 nm are needed to design effective magnetic nanoparticles in one-pot for MIAs.

Here, we demonstrate a one-pot synthesis and a systematic design and characterization of five different types of MNCs containing either Zn and Fe, Co and Fe, or Co, Zn and Fe. We show how to vary metal ion concentration in the synthesis to obtain the right size and shape of the NCs along with the magnetic properties needed. Our best performing MNCs contain Co, Zn and Fe as the key components. For an ultrahigh sensitivity, our synthetic protocol enables us to interchangeably tune the amount of cobalt and zinc doping while keeping the particle size within the optimal size range of 20-25 nm.

RESULTS AND DISCUSSION:

The particle design is based on our previous expertise and results, where we have demonstrated the impact of synthesis conditions on size and shape of the particles.[22] Other studies have shown that the choice of surfactant types also plays a crucial role in the size, shape, and growth of the particles.[13,16,23,24] Here, we have optimized four crucial synthesis parameters: feed ratio of dopants, choice of solvents to stabilize growth temperature, choice of surfactants to control the shape, and heating ramp rate to favour nucleation and growth of the particles (for details see SI). We synthesized both binary and ternary magnetic particles of different sizes with a varying amount of Co and/or Zn dopants to unravel the interplay between particle size, composition, and magnetic properties. The particles span a size range from 8 nm to 50 nm (Table 1). We first investigated the morphology, size, and size distribution of all the particles using transmission electron microscopy (TEM) (Figure 1a-e). We find that all the particles except one with highest Zn doping are highly monodisperse with no change in their cubic structures. The particle size histograms were fitted with a Gaussian distribution function

shown in the lower panels (Figure 1). The size distribution analysis showed that the solely Zn and Co doped NCs have the narrowest size distribution among all, suggesting that the growth of the nanocubes under thermal decomposition is influenced by the amount, type, and competition between the doping ions.

As Zn doping increases the particle size dramatically,[22] we use 0.25 mol equivalent of Zn for 1.0 mol equivalent of Fe. This produced about 8.1±0.6 nm NCs. To synthesize cobalt-ferrite particles of a bigger size than the zinc-ferrite particles, we use 0.50 mol equivalent of Co for 1.0 mol equivalent of Fe. Thus, we obtained 15.8±1.2 nm NCs. These two particles set a base to systematically synthesize the ternary NCs bigger than the binary NCs by employing all the three ions with a mol ratio of 0.25:0.50:1.0 for Zn, Co, and Fe, respectively. As a result, we obtained 20±1.7 nm NCs (see Table 1). The successful preparation of the first ternary NCs (CFZ1) motivated us to then increase the amount of Zn. Accordingly, to synthesize ternary NCs bigger than 20 nm, we employed 0.5 and 0.75 mol equivalents of Zn with respect to 1.0 mol equivalent of Fe, while keeping the 0.5 mol equivalent of Co constant for both types. With the mol ratio of 0.50:0.50:1.0, respectively for Zn, Co, and Fe, we acquired 25.4±3.3 nm NCs (CFZ2). However, the doping of 0.75 mol equivalent of Zn tends to yield significantly bigger NCs of > 52 nm (CFZ3). The ICP-OES data suggests that although the amounts of Zn and Co increase linearly with the doping level (Table 1), the size of the particles do not follow a linear growth above 25 nm, meaning there is a limit of Zn doping for a linear growth of the particles. Furthermore, we find that CFZ3 particles are not colloidally stable as they quickly sediment in chloroform after they are homogeneously dispersed by sonication. To probe the distribution of Fe, Co and Zn of NCs, we carried out energy dispersive X-ray on the CF and CFZ1 NCs. Both particles revealed a uniform distribution of elements throughout the particle (Figure 1f-g).

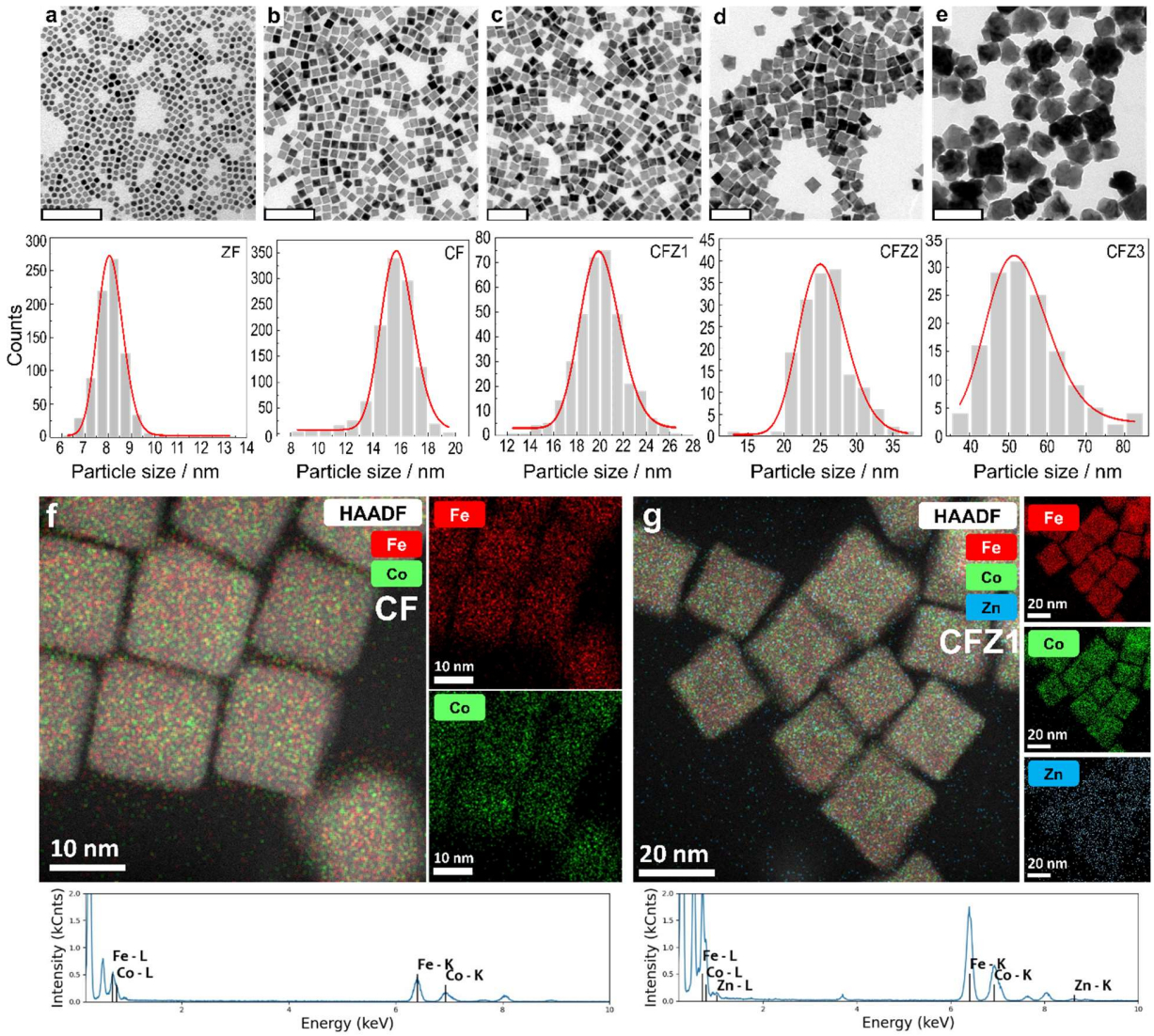

Figure 1. TEM, high angle annular dark field-scanning transmission electron microscopy (HAADF-STEM), and energy dispersive X-ray (EDX) studies of the MNCs. Top panel (a-e) shows the TEM micrographs of ZF, CF, CFZ1, CFZ2, and CFZ3 particles, respectively, from left to right. Scale bars, 100 nm. The panel below shows the corresponding size histogram of the particles. The HAADF-STEM and EDX (f-g) were performed on two exemplary Brownian relaxing particles. The panel (f) shows the overlay of Fe and Co EDX elemental maps of the CF NCs, showing a uniform distribution and colocalization of both elements on the particles. The panel (g) depicts the overlay of Fe, Co, and Zn EDX elemental maps of the CFZ1 NCs, revealing a homogenous distribution of all three metal elements throughout the particles. The panel below f-g shows the EDX spectra of the corresponding particles, indicating the presence of Fe, Co, and Zn elements at their expected binding energy. The spectroscopy measurements performed on these two samples show no detectable phase segregation and/or compositional inhomogeneity at the nanoscale.

We next investigated static and dynamic magnetic properties of the synthesized particles. The magnetization hysteresis loops measured at 298 K revealed several interesting features (Figure 2a). First, the binary ZF and CF NCs possess the highest and lowest magnetisation M_{max} values of ≈ 80 and ≈ 40 A·m²/kg$_{MNC}$, respectively. It is well known that when Zn^{2+} ions sit on the tetrahedral (A) crystalline sites in the iron oxide crystal structure giving the chemical formula of $(Zn^{2+}Fe^{3+})_x^A(Fe^{2+},Fe^{3+})_{3-x}^BO_4$, it reduces the antiferromagnetic coupling between Fe^{3+} in the tetrahedral and octahedral sites and increases the *M* value. Comparing the M_{max} value of 9 nm iron oxide nanoparticles with one of ZF NCs, an increase of ≈ 30 A·m²/kg$_{MNC}$ as a result of Zn doping can be appreciated.[13] However, Cobalt shows a different characteristic. In the inverse spinel structure of cobalt ferrite, Co^{2+} ions mainly sit on the octahedral (B) crystalline sites, giving

$(Fe^{3+})_x^A(Co^{2+},Fe^{2+},Fe^{3+})_{3-x}^BO_4$ as the most probable chemical formula. The Co doping results in the reduction of M_{max} owing to its lower magnetic moment per spin i.e. 3 μ_B. This phenomenon accounts for the lowest M_{max} recorded for the CF NCs with 0.85 Co^{2+} substitution for Fe^{2+}. Second, in line with this discussion, the ternary CFZ1, CFZ2, and CFZ3 NCs showed an expected trend, in which CFZ3 with the highest Zn^{2+} and lowest Co^{2+} doping level have the highest M_{max} among them. Looking closer at the low magnetic field region of the hysteresis loops (Figure 2b), it can be discerned that the ZF NCs possess no coercive fields H_c, revealing their soft magnetic and low anisotropy constant characteristics. Third, remarkably, the ternary CFZ1, CFZ2, and CFZ3 samples have comparable H_c values despite having different particle sizes, indicating that all the CFZ NCs have a comparable anisotropy constant K.

The correlation between M and magnetic relaxation mechanism in ternary magnetic nanoparticles is far from trivial and yet poorly understood. It is therefore of highest importance to study the magnetic relaxation mechanism of the particles at both linear and non-linear magnetization regimes. To do so, we first measured the complex alternating current (AC) susceptibility (ACS) on colloidal suspensions of the particles (Figures 2c and 2d). The measurements were performed at a magnetic field of $\mu_0 H$ = 95 μT and frequencies up to a few hundreds of kHz, probing the linear magnetic susceptibility of the particles.[25] Particles relaxing via the Brownian mechanism show a peak in the imaginary part χ'' of ACS at the angular frequency of $\omega = 1/\tau_B$, with τ_B the Brownian relaxation time constant (details are given in SI). The ZF NCs showed no relaxation peak, indicating that they experience no difficulties in following the AC magnetic field up to the highest frequency measured (Figure 2d). This result indicates that their dominant relaxation mechanism is Néel, which can be attributed to their 8 nm particle size and soft magnetic nature. In contrast, the CF NCs revealed a pronounced Brownian relaxation peak at the frequency of ≈ 53 kHz. The Brownian relaxation peaks of the CFZ1 and CFZ2 NCs lie at ≈ 22 and 11 kHz, respectively. The CFZ3 NCs did not generate a good spectrum as they aggregate and sediment quickly in the sample holder because of their larger sizes and strong interparticle magnetic interactions. However, the relaxation peak of the CFZ3 NCs appears to be at frequencies < 200 Hz.

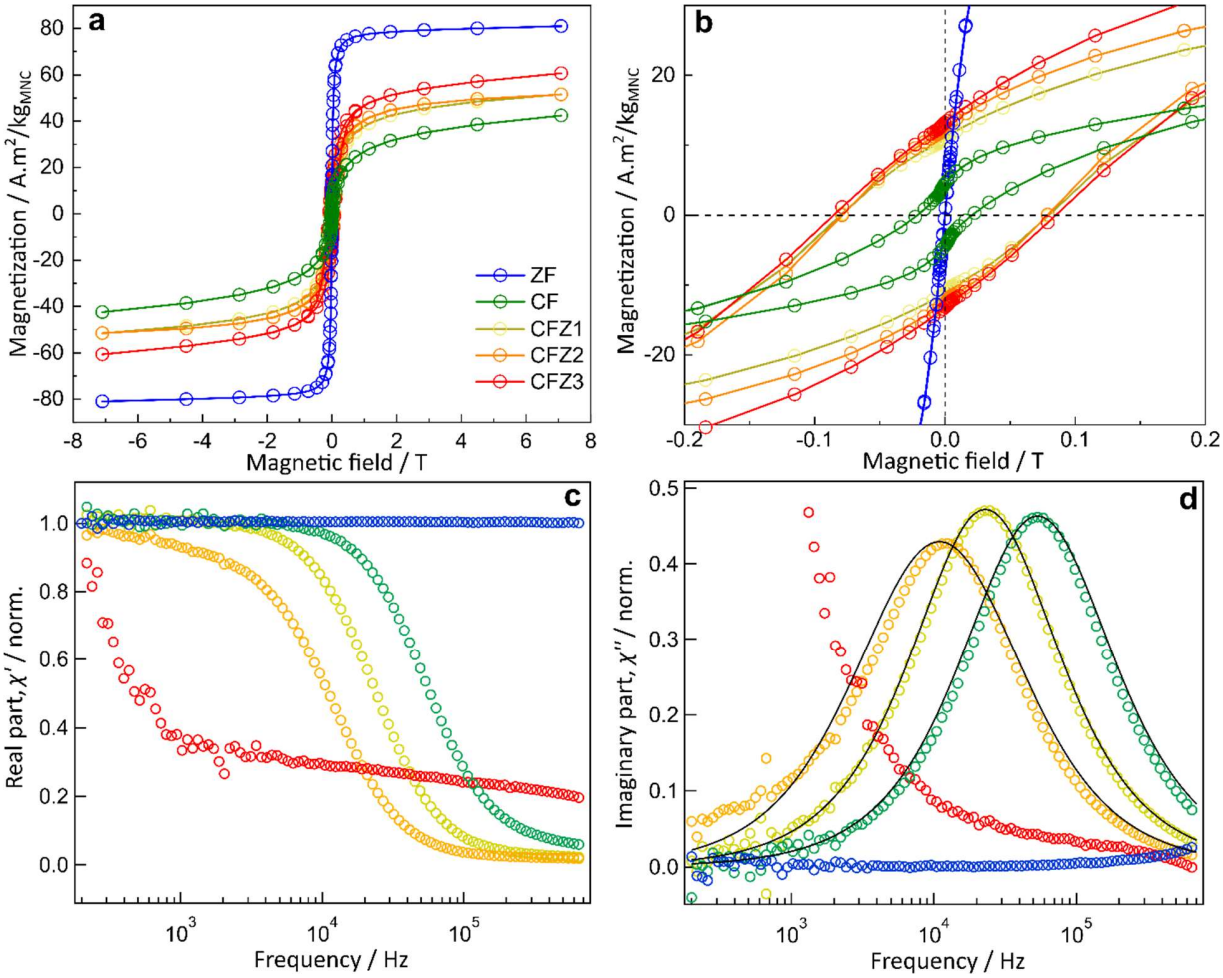

Figure 2. Magnetization hysteresis loops and ac susceptibility measurements on all the samples. Panels (a) and (b) show magnetic hysteresis loops measured between – 7 T and 7 T at room temperature in a vibrating sample magnetometer (VSM) mode using magnetic property measurement system (MPMS3, Quantum Design) on dried particles. The magnetization curves are normalized to the particle concentration. Panels (c) and (d) show the real and imaginary parts of complex alternating current susceptibility (ACS) recorded at 295 K and the field amplitude of $\mu_0 H$ = 95 μT on particle suspensions in chloroform. The data is normalized to χ_0 (Eq. 2) (see SI). The black lines in the panel (d) are the best fits obtained using the Eq. 2 and fit parameters summarized in table 1. Same color coding is applied to all the panels.

For perfectly monodisperse nanoparticles relaxing thoroughly via the Brownian mechanism, the nominal ratio of $\boldsymbol{\chi''}$ to $\boldsymbol{\chi_0}$ at $\boldsymbol{\omega\tau_B = 1}$ is equal to 0.5, with $\boldsymbol{\chi_0}$ the static susceptibility. This ratio decreases due to particle size distribution, the presence of a fraction of Néel relaxing particles, particle-particle interactions, and agglomeration. Therefore, this ratio can be used as a reliable and qualitative indicator to compare different samples in terms of their suitability for MIAs. The $\boldsymbol{\chi''/\chi_0}$ ratio reads 0.46, 0.47, and 0.43 for the CF, CFZ1, and CFZ2 NCs, respectively, revealing that CFZ1 NCs are the most Brownian relaxing particles among them. Moreover, the ACS data can also be utilized to get the hydrodynamic size of the

particles. We modelled the χ'' part of the ACS spectra recorded on the CF, CFZ1, and CFZ2 NCs using Debye model (solid lines in Figure 2d, see SI for details) to extract the particle hydrodynamic size distribution (see table 1). It is remarkable to mention that the difference between the particle core size (measured by TEM) and d_h (extracted from the fits) for these three samples lies between 3.5 nm and 7.2 nm, matching the expected size increase due to a single layer of oleic acid on particles having a nominal length of ≈ 2-2.5 nm.[26]

To understand particle magnetization dynamics at magnetic field conditions relevant for MIAs, we next characterized the particles at two different frequencies using magnetic particle spectrometer (MPS).[27] By converting magnetization curve from the time domain to the frequency domain using Fourier-transform, the MPS higher harmonics spectrum is appeared (Figure 3). Looking at Fig. 3a that shows the MPS harmonics spectra of all samples at 1 kHz, several features can be discerned. First, the amplitude of the fundamental frequency, that is to say the excitation AC field, follows the same order like the M_{max} values (table 1), i.e. ZF > CFZ3 > CFZ2 ≥ CFZ1 > CF with the CFZ3 NCs as the only exception. Second, the ZF and CF NCs, having the smallest particle size and thus magnetic moment per particle, derived from TEM and M(H) studies, revealed the steepest drop in the harmonics amplitudes. In contrast to ZF and CF, the CFZ2 and CFZ1 NCs with the largest magnetic moment per particle exhibited the richest harmonics spectrum among all the samples, staying up to the 30th harmonics above the noise level. The effect of dynamics can be clearly seen by increasing the excitation frequency. By increasing the excitation frequency from 1 kHz to 10 kHz, the harmonics spectra of the ZF and CF NCs remained unchanged, matching the ACS results (Figure 3b). In contrast, the ternary NCs showed noticeable changes by increasing the excitation frequency to 10 kHz. The 3rd and 5th MPS harmonics amplitudes decreases with the excitation frequency for all ternary particles. The harmonics spectra of the CFZ1 is least influenced at 10 kHz among all the ternary samples. The ratio of the 3rd and 5th MPS harmonics amplitudes, often used in MPS-based MIAs as the binding indicator,[28] is higher at the lower frequency, indicating that the optimal frequency for the CFZ1 NCs lies at around 1 kHz at 25 mT.

Putting TEM, MPMS, ACS, and MPS results together, we can infer that the ternary CFZ1 NCs are the most promising particle system for MIAs. Therefore, we investigated the magnetization dynamics and detection sensitivity of CFZ1 after transferring them to water with catechol-based PEG ligands. The catechol-PEG ligand synthesis (see SI) was carried out with some modifications of our previous protocol.[29] TEM imaging shows that the CFZ1 particles preserve the single-particle resolution after ligand exchange (Figure 4a). The dynamic light scattering (DLS) analyses (Figure 4b) reveal their excellent colloidal stability over a month in PBS buffer. However, the hydrodynamic diameter of the CFZ1 NCs in PBS becomes ≈ 3.5 times bigger than its core diameter. This we attribute to PEG coating which was also demonstrated by Xie et. al.[26] To determine the particle limit-of-detection (LOD), a concentration series was measured with the particles dispersed in PBS buffer (Figure 4c-d). Plotting the MPS 3rd harmonics amplitude *vs*. particle concentration (Fig. S1) and applying 3σ criterion, we find that the LOD of the water dispersed $Zn_{0.06}Co_{0.80}Fe_{2.14}O_4$ NCs is ≈ 0.6 femtomole, which corresponds to ≈ 0.3 µg/ml or ≈ 10 pM of particles. The combination of our particle system and immunoMPS setup offers three orders of magnitude better particle LOD compared to what was reported for commercial single-core particles of comparable size employing a frequency-mixing MPS setup,[30] eventually leading to ultrasensitive analyte detection.

Table 1. Feed and final compositions of Zn, Co, and Fe in the particles, the particle and hydrodynamic sizes d_h, maximum magnetization M_{max}, and coercive field H_c values at 298 K, as derived from ICP-OES, TEM, ac-susceptibility, and magnetization hysteresis loops measurements and analyses.

Nanocubes (NCs)	Fe/Co/Zn (feed ratio in mmol)	NCs composition (based on ICP)	NCs size (nm)	d_h, σ_h (nm)	H_c (mT)	M_{max} (A·m²/kg$_{MNC}$)
ZF	1.0/0/0.25	$Zn_{0.1}Fe_{2.9}O_4$	8.1 ± 0.6	---	0.1	80.9
CF	1.0/0.5/0	$Co_{0.85}Fe_{2.15}O_4$	15.8 ± 1.2	19.3, 0.1	20.9	42.4
CFZ1	1.0/0.5/0.25	$Zn_{0.06}Co_{0.80}Fe_{2.14}O_4$	20.0 ± 1.7	25.5, 0.1	79.9	51.6
CFZ2	1.0/0.5/0.50	$Zn_{0.12}Co_{0.75}Fe_{2.13}O_4$	25.4 ± 3.3	32.6, 0.2	78.7	51.5
CFZ3	1.0/0.5/0.75	$Zn_{0.19}Co_{0.69}Fe_{2.12}O_4$	52.6 ± 8.1	---	85.2	60.6

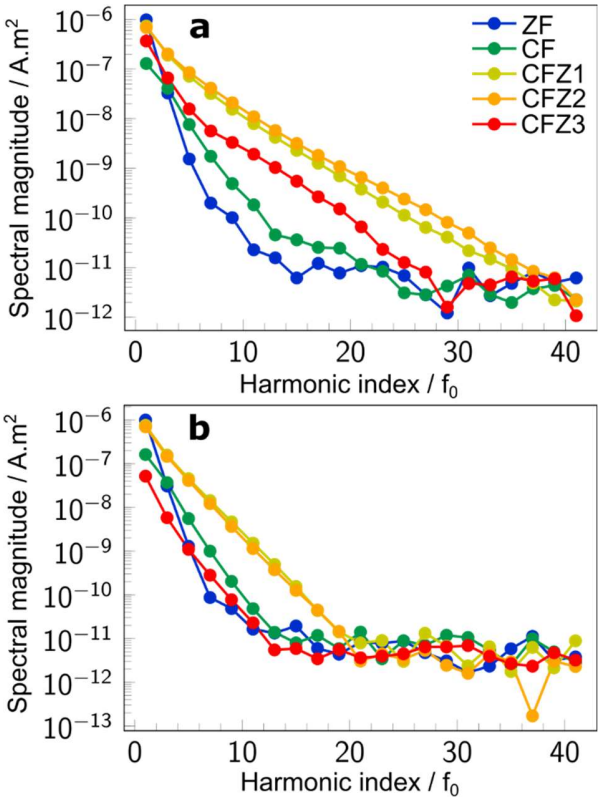

Figure 3. Magnetic particle spectroscopy (MPS) characterization of all the samples in chloroform. Panels (a) and (b) show the MPS harmonics spectra of all the samples at 1 kHz and 10 kHz, respectively. The spectra shown in panels (a and b) are measured on samples at a particle concentration of 3 mg/mL and are therefore normalized to the particle concentration. The magnetic field amplitude for all the measurements is $\mu_0 H$ = 25 mT. Same color coding is applied to panels (a) and (b).

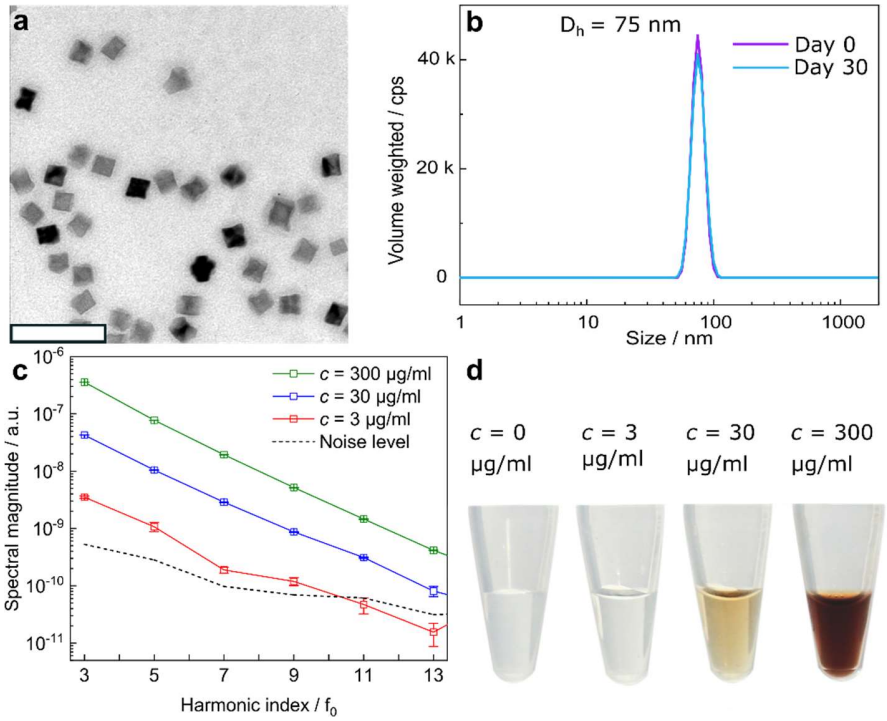

Figure 4. Characterization of PEG-coated CFZ1 NCs dispersed in PBS. Panels (a) and (b) show the TEM image of NCs and their volume weighted hydrodynamic size distribution (DLS) at days 0 and 30 in PBS (pH 7.4, 200 mM NaCl), respectively. Panel (c) shows the harmonics spectra at different particle concentrations in PBS. The MPS harmonics spectra were measured using a custom-made Immuno-MPS setup operating at an excitation frequency of 590 Hz and field amplitude of $\mu_0 H$ = 15 mT. The dotted grey line shows the noise level of the measurements. Error bars correspond to standard deviation for n=3 measurements. Panel (d) shows the digital photograph of NCs dispersed in PBS 7.4 at different particle concentrations. Scale bar in panel (a) is 100 nm.

CONCLUSION. Here, we demonstrate that the size and composition of the particles can be precisely tuned by varying the amount of Zn doping, while keeping the Co and Fe feed ratio as 0.5:1. ACS measurements demonstrated that $Zn_{0.1}Fe_{2.9}O_4$ particles are thoroughly Néel relaxing. In contrast, all other particles containing Co, Zn, and Fe are Brownian relaxing. The most Brownian relaxing particles, judged by the χ''/χ_0 ratio from the ACS analyses, are ≈ 20 nm $Zn_{0.06}Co_{0.80}Fe_{2.14}O_4$. Under applied AC fields, the ternary particles showed higher MPS harmonics numbers compared to binary particles. Interestingly, despite possessing the highest M_s among all, the Néel relaxing particles did not generate rich MPS spectrum compared to the cobalt-zinc-ferrite particles. We found that the interplay between particle size and doping of Zn and Co determines the particle suitability for high sensitivity and MPS-based magnetic immunoassays. Measured by our custom-built immunoMPS spectrometer, the 20 nm tri-component nanoparticles achieved three orders of magnitude better particle LOD than commercial nanoparticles of comparable size. Furthermore, we demonstrated that the ternary particles can be transferred to aqueous media at a single particle resolution by employing our catechol-based PEG ligands. DLS studies of water-dispersed particles showed long-term stability in PBS over a month without any aggregation. Using heterofunctional PEG, the ternary NCs can be transferred to water for further functionalization, enabling them to be a modular platform to graft different biomolecules for specific assays. Further, the detection limit can be improved collectively by reducing the sample volume and improving particle properties. Our systematic studies on single-core particles will set a solid foundation to establish mix-and-measure, quantitative, and ultrahigh sensitive MPS-based magnetic immunoassays.

AUTHOR INFORMATION

Corresponding Author

*Aidin Lak, Email: a.lak@tu-braunschweig.de.

Author Contributions

M.S.C. and A.L. designed the research; M.S.C. synthesized the magnetic nanoparticles and catechol-PEG ligands, analyzed the data and wrote the manuscript; E.L.R. performed the magnetization measurements, ImmunoMPS-based experiments, and analyzed the data. K.-J.J. performed the MPS-based experiments and analyzed the data. F.W. and T.V. jointly built the bench-top ImmunoMPS. D.A.E and S.B. performed the HAADF-STEM and EDX measurements and analyzed the data. T.V. and F.L. analyzed the data and contributed to the writing. M.S. contributed to the magnetic analysis. A.L. performed the TEM measurements, supervised the study, analyzed the data, and wrote the manuscript. All authors have given approval to the final version of the manuscript.

SUPPORTING INFORMATION

Experimental details as mentioned in the text including: nanoparticle synthesis, catechol-PEG ligand synthesis, and detailed characterization of particles. Modelling of ACS spectra, LOD determination of particles, and picture of experimental setup for particle synthesis.

ACKNOWLEDGMENT

This work is supported by the German Research Foundation DFG (DFG RTG 1952 “NanoMet”), Junior Research Group “Metrology4life”, and the add-on fellowship of Joachim Herz Foundation. We acknowledge Petra Schmidt (TU Braunschweig) for ICP-OES measurements, Prof. Tim Liedl (LMU, Munich) for TEM facilities, and Chris Pauer (LMU Munich) for assisting in TEM imaging of water-based nanoparticles. For HAADF-STEM and spectroscopy experiments, this project has received funding from the European Union’s Horizon 2020 research and innovation programme under grant agreement No. 823717 – ESTEEM3.

REFERENCES

(1) Wu, K.; Su, D.; Saha, R.; Wong, D.; Wang, J. P. Magnetic Particle Spectroscopy-Based Bioassays: Methods, Applications, Advances, and Future Opportunities. *J. Phys. D. Appl. Phys.* **2019**, *15* (17), 173001. https://doi.org/10.1088/1361-6463/ab03c0.

(2) Guteneva, N. V.; Znoyko, S. L.; Orlov, A. V.; Nikitin, M. P.; Nikitin, P. I. Rapid Lateral Flow Assays Based on the Quantification of Magnetic Nanoparticle Labels for Multiplexed Immunodetection of Small Molecules: Application to the Determination of Drugs of Abuse. *Microchim. Acta* **2019**, *186* (9), 621. https://doi.org/10.1007/s00604-019-3726-9.

(3) Orlov, A. V.; Znoyko, S. L.; Cherkasov, V. R.; Nikitin, M. P.; Nikitin, P. I. Multiplex Biosensing Based on Highly Sensitive Magnetic Nanolabel Quantification: Rapid Detection of Botulinum Neurotoxins A, B, and e in Liquids. *Anal. Chem.* **2016**, *88* (21), 10419–10426. https://doi.org/10.1021/acs.analchem.6b02066.

(4) Lu, W.; Chen, Y.; Liu, Z.; Tang, W.; Feng, Q.; Sun, J.; Jiang, X. Quantitative Detection of MicroRNA in One Step via Next Generation Magnetic Relaxation Switch Sensing. *ACS Nano* **2016**, *10* (7), 6685–6692. https://doi.org/10.1021/acsnano.6b01903.

(5) Demortière, A.; Panissod, P.; Pichon, B. P.; Pourroy, G.; Guillon, D.; Donnio, B.; Bégin-Colin, S. Size-Dependent Properties of Magnetic Iron Oxide Nanocrystals. *Nanoscale* **2011**, *3* (1), 225–232. https://doi.org/10.1039/c0nr00521e.

(6) Rocha-Santos, T. A. P. Sensors and Biosensors Based on Magnetic Nanoparticles. *TrAC - Trends Anal. Chem.* **2014**, *62*, 28–36. https://doi.org/10.1016/j.trac.2014.06.016.

(7) Dieckhoff, J.; Lak, A.; Schilling, M.; Ludwig, F. Protein Detection with Magnetic Nanoparticles in a Rotating Magnetic Field. *J. Appl. Phys.* **2014**, *115* (2), 024701. https://doi.org/10.1063/1.4861032.

(8) Zhu, X.; Li, J.; Peng, P.; Hosseini Nassab, N.; Smith, B. R. Quantitative Drug Release Monitoring in Tumors of Living Subjects by Magnetic Particle Imaging Nanocomposite. *Nano Lett.* **2019**, *19* (10), 6725–6733. https://doi.org/10.1021/acs.nanolett.9b01202.

(9) Aslibeiki, B.; Kameli, P.; Salamati, H.; Concas, G.; Fernandez, M. S.; Talone, A.; Muscas, G.; Peddis, D. Co-Doped MnFe2O4 Nanoparticles: Magnetic Anisotropy and Interparticle Interactions. *Beilstein J. Nanotechnol.* **2019**, *10*, 856–865. https://doi.org/10.3762/BJNANO.10.86.

(10) Byrne, J. M.; Coker, V. S.; Moise, S.; Wincott, P. L.; Vaughan, D. J.; Tuna, F.; Arenholz, E.; Van Der Laan, G.; Pattrick, R. A. D.; Lloyd, J. R.; Telling, N. D. Controlled Cobalt Doping in Biogenic Magnetite Nanoparticles. *J. R. Soc. Interface* **2013**, *10* (83), 1. https://doi.org/10.1098/rsif.2013.0134.

(11) Sathya, A.; Guardia, P.; Brescia, R.; Silvestri, N.; Pugliese, G.; Nitti, S.; Manna, L.; Pellegrino, T. CoxFe3-XO4 Nanocubes for Theranostic Applications: Effect of Cobalt Content and Particle Size. *Chem. Mater.* **2016**, *28* (6), 1769–1780. https://doi.org/10.1021/acs.chemmater.5b04780.

(12) Tatarchuk, T.; Bououdina, M.; Macyk, W.; Shyichuk, O.; Paliychuk, N.; Yaremiy, I.; Al-Najar, B.; Pacia, M. Structural, Optical, and Magnetic Properties of Zn-Doped CoFe2O4 Nanoparticles. *Nanoscale Res. Lett.* **2017**, *12* (1), 141. https://doi.org/10.1186/s11671-017-1899-x.

(13) Silvestri, N.; Gavilán, H.; Guardia, P.; Brescia, R.; Fernandes, S.; Samia, A. C. S.; Teran, F. J.; Pellegrino, T. Di- And Tri-Component Spinel Ferrite Nanocubes: Synthesis and Their Comparative Characterization for Theranostic Applications. *Nanoscale* **2021**, *13* (32), 13665–13680. https://doi.org/10.1039/d1nr01044a.

(14) Sartori, K.; Choueikani, F.; Gloter, A.; Begin-Colin, S.; Taverna, D.; Pichon, B. P. Room Temperature Blocked Magnetic Nanoparticles Based on Ferrite Promoted by a Three-Step Thermal Decomposition Process. *J. Am. Chem. Soc.* **2019**, *141* (25), 9783–9787. https://doi.org/10.1021/jacs.9b03965.

(15) Lee, J. H.; Jang, J. T.; Choi, J. S.; Moon, S. H.; Noh, S. H.; Kim, J. W.; Kim, J. G.; Kim, I. S.; Park, K. I.; Cheon, J. Exchange-Coupled Magnetic Nanoparticles for Efficient Heat Induction. *Nat. Nanotechnol.* **2011**, *6* (7), 418–422. https://doi.org/10.1038/nnano.2011.95.

(16) Muro-Cruces, J.; Roca, A. G.; López-Ortega, A.; Fantechi, E.; Del-Pozo-Bueno, D.; Estradé, S.; Peiró, F.; Sepúlveda, B.; Pineider, F.; Sangregorio, C.; Nogues, J. Precise Size Control of the Growth of Fe3O4 Nanocubes over a Wide Size Range Using a Rationally Designed One-Pot Synthesis. *ACS Nano* **2019,** *13* (7), 7716-7728. https://doi.org/10.1021/acsnano.9b01281.

(17) Krishnan, K. M. Biomedical Nanomagnetics: A Spin through Possibilities in Imaging, Diagnostics, and Therapy. *IEEE Trans. Magn.* **2010**, *46* (7), 2523–2558. https://doi.org/10.1109/TMAG.2010.2046907.

(18) Yu, W. W.; Falkner, J. C.; Yavuz, C. T.; Colvin, V. L. Synthesis of Monodisperse Iron Oxide Nanocrystals by Thermal Decomposition of Iron Carboxylate Salts. *Chem. Commun.* **2004**, No. 20, 2306–2307. https://doi.org/10.1039/b409601k.

(19) Park, J.; An, K.; Hwang, Y.; Park, J. E. G.; Noh, H. J.; Kim, J. Y.; Park, J. H.; Hwang, N. M.; Hyeon, T. Ultra-Large-Scale Syntheses of Monodisperse Nanocrystals. *Nat. Mater.* **2004**, *3* (12), 891–895. https://doi.org/10.1038/nmat1251.

(20) Guardia, P.; Di Corato, R.; Lartigue, L.; Wilhelm, C.; Espinosa, A.; Garcia-Hernandez, M.; Gazeau,

F.; Manna, L.; Pellegrino, T. Water-Soluble Iron Oxide Nanocubes with High Values of Specific Absorption Rate for Cancer Cell Hyperthermia Treatment. *ACS Nano* **2012**, *6* (4), 3080–3091. https://doi.org/10.1021/nn2048137.

(21) Guardia, P.; Riedinger, A.; Nitti, S.; Pugliese, G.; Marras, S.; Genovese, A.; Materia, M. E.; Lefevre, C.; Manna, L.; Pellegrino, T. One Pot Synthesis of Monodisperse Water Soluble Iron Oxide Nanocrystals with High Values of the Specific Absorption Rate. *J. Mater. Chem. B* **2014**, *2* (28), 4426–4434. https://doi.org/10.1039/c4tb00061g.

(22) Lak, A.; Kahmann, T.; Schaper, S. J.; Obel, J.; Ludwig, F.; Müller-Buschbaum, P.; Lipfert, J. The Dissociation Rate of Acetylacetonate Ligands Governs the Size of Ferrimagnetic Zinc Ferrite Nanocubes. *ACS Appl. Mater. Interfaces* **2020**, *12* (1), 217–226. https://doi.org/10.1021/acsami.9b17714.

(23) Baaziz, W.; Pichon, B. P.; Liu, Y.; Grenèche, J. M.; Ulhaq-Bouillet, C.; Terrier, E.; Bergeard, N.; Halté, V.; Boeglin, C.; Choueikani, F.; Toumi, M.; Mhiri, T.; Begin-Colin, S. Tuning of Synthesis Conditions by Thermal Decomposition toward Core-Shell CoxFe1- XO@CoyFe3- YO4 and CoFe2O4 Nanoparticles with Spherical and Cubic Shapes. *Chem. Mater.* **2014**, *26* (17), 5063–5073. https://doi.org/10.1021/cm502269s.

(24) Mameli, V.; Musinu, A.; Ardu, A.; Ennas, G.; Peddis, D.; Niznansky, D.; Sangregorio, C.; Innocenti, C.; Thanh, N. T. K.; Cannas, C. Studying the Effect of Zn-Substitution on the Magnetic and Hyperthermic Properties of Cobalt Ferrite Nanoparticles. *Nanoscale* **2016**, *8* (19), 10124–10137. https://doi.org/10.1039/c6nr01303a.

(25) Ludwig, F.; Guillaume, A.; Schilling, M.; Frickel, N.; Schmidt, A. M. Determination of Core and Hydrodynamic Size Distributions of CoFe 2O4 Nanoparticle Suspensions Using Ac Susceptibility Measurements. *J. Appl. Phys.* **2010**, *108* (3). https://doi.org/10.1063/1.3463350.

(26) Xie, J.; Xu, C.; Kohler, N.; Hou, Y.; Sun, S. Controlled PEGylation of Monodisperse Fe3O4 Nanoparticles for Reduced Non-Specific Uptake by Macrophage Cells. *Adv. Mater.* **2007**, *19* (20), 3163–3166. https://doi.org/10.1002/adma.200701975.

(27) Draack, S.; Lucht, N.; Remmer, H.; Martens, M.; Fischer, B.; Schilling, M.; Ludwig, F.; Viereck, T. Multiparametric Magnetic Particle Spectroscopy of CoFe2O4 Nanoparticles in Viscous Media. *J. Phys. Chem. C* **2019**, *123* (11), 6787–6801. https://doi.org/10.1021/acs.jpcc.8b10763.

(28) Rösch, E. L.; Zhong, J.; Lak, A.; Liu, Z.; Etzkorn, M.; Schilling, M.; Ludwig, F.; Viereck, T.; Lalkens, B. Point-of-Need Detection of Pathogen-Specific Nucleic Acid Targets Using Magnetic Particle Spectroscopy. *Biosens. Bioelectron.* **2021**, *192*, 113536. https://doi.org/10.1016/j.bios.2021.113536.

(29) Lak, A.; Dieckhoff, J.; Ludwig, F.; Scholtyssek, J. M.; Goldmann, O.; Lünsdorf, H.; Eberbeck, D.; Kornowski, A.; Kraken, M.; Litterst, F. J.; Fiege, K.; Mischnick, P.; Schilling, M. Highly Stable Monodisperse PEGylated Iron Oxide Nanoparticle Aqueous Suspensions: A Nontoxic Tracer for Homogeneous Magnetic Bioassays. *Nanoscale* **2013**, *5* (23), 11447–11455. https://doi.org/10.1039/c3nr02197a.

(30) Wu, K.; Liu, J.; Saha, R.; Su, D.; Krishna, V. D.; Cheeran, M. C. J.; Wang, J. P. Magnetic Particle Spectroscopy for Detection of Influenza A Virus Subtype H1N1. *ACS Appl. Mater. Interfaces* **2020**, *12* (12), 13686–13697. https://doi.org/10.1021/acsami.0c00815.

SYNOPSIS TOC